Fermi-surface-induced lattice distortion in NbTe₂

Corsin Battaglia,* Hervé Cercellier, Florian Clerc, Laurent Despont, Michael Gunnar Garnier, Christian Koitzsch,[†] and
Philipp Aebi

Institut de Physique, Université de Neuchâtel, CH-2000 Neuchâtel, Switzerland

Helmuth Berger and László Forró

Institute of Physics of Complex Matter, EPFL, CH-1015 Lausanne, Switzerland

Claudia Ambrosch-Draxl

Institut für Physik, Karl-Franzens-Universität Graz, A-8010 Graz, Austria

The origin of the monoclinic distortion and domain formation in the quasi-two-dimensional layer compound NbTe₂ is investigated. Angle-resolved photoemission shows that the Fermi surface is pseudogapped over large portions of the Brillouin zone. *Ab initio* calculation of the electron and phonon band structure as well as the static RPA susceptibility lead us to conclude that Fermi surface nesting and electron-phonon coupling play a key role in the lowering of the crystal symmetry and in the formation of the charge density wave phase.

I. INTRODUCTION

NbTe₂ belongs to the category of layered transition metal dichalcogenides (TMDCs) known for their quasi-two-dimensional (2D) properties. Due to the reduced dimensionality, free charge carriers and phonons are coupling in an unique fashion, leading to the formation of charge density waves (CDWs) and superconductivity.

The competition between these two electronic ground-states is especially interesting in view of the anomalous properties of another class of strongly anisotropic layered materials, the high-T_c cuprate superconductors. Attempts to explain the complexity of electronic and magnetic properties observed in these compounds are based on the subtle balancing of competing interactions producing superconducting pairing, spin and charge ordering. For NbTe₂, magnetic degrees of freedom are unlikely to play an important role. Thus, in principle, NbTe₂ allows one to isolate the effects associated with density wave instabilities and superconductivity. An explanation for the CDW transition in 2D materials is derived from the theory for the Peierls instability[1] in 1D metals. A system of conduction electrons may under suitable conditions become unstable with respect to a spatially modulated perturbation with wave vector **q**, such as a static periodic lattice distortion. Kohn[2] has shown that such soft phonon modes may result from the screening of lattice vibrations by conduction electrons. According to linear response theory, the quality of the screening by the electrons is measured by the static generalized susceptibility with Fourier component $\chi(\mathbf{q})$. Instability sets in when this quantity diverges. This happens under favorable nesting conditions for which large portions of the Fermi surface can be connected or nested by a single **q** vector. Even when the system is not truly one-dimensional, nesting may become important, if the Fermi surface consists of flat parallel sheets. However, 2D systems often remain metallic, since the opening of the gap removes only parts of the Fermi surface.

The distortion already observed at room temperature in NbTe₂ and the isostructural TaTe₂ suggests the action of a single-axis CDW. The structure[3] is a monoclinically deformed version of the trigonal 1*T* polytype, in which the transition metal sits in octahedrally coordinated sites between the chalcogen atoms (see the Appendix for structural details). The metal atoms are displaced from the center of the coordination unit and the chalcogen layers form zigzag chains to accomodate these shifts (see Fig. 1). After cooling of heat pulsed crystals to room temperature, transmission electron diffraction experiments revealed a second, seemingly unrelated triple-axis CDW state with a $(\sqrt{19} \times \sqrt{19})$ signature,[4–6] commensurate at room temperature, but readily rendered incommensurate just above.

NbTe₂ and TaTe₂ are semimetals.[7] The resistivity decreases monotonically with decreasing temperature.[8–10] A drop in resistivity of NbTe₂ in the range 0.5−0.74 K marks the transition into the superconducting phase.[11] Superconductivity is absent in TaTe₂.[12]

After a discussion of the experimental and theoretical methods, we will investigate the interplay between electronic and structural properties of NbTe₂. Our low-energy electron diffraction (LEED) measurements will allow an alternative
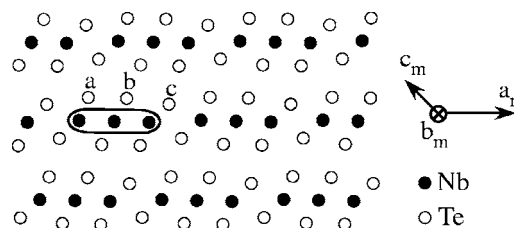

FIG. 1. Side view of the monoclinic structure of NbTe₂ [projection onto the (010) plane within the monoclinic space group]. Each layer of NbTe₂ consists of a Te-Nb-Te sandwich. The Nb atoms (filled circles) are displaced within the plane and form "trimers," whereas the Te atoms (empty circles) exhibit an out-of-plane buckling (a,b,c). Successive Te-Nb-Te sandwiches are shifted within the plane. The stacking sequence is repeated after three layers.

parametrization of the structure proposed by x-ray diffraction measurements, which is more appropriate in the discussion of electron dynamics. Numerous studies of the electronic properties have been carried out for disulfides[13–21] and diselenides.[16,18,22–24] Direct measurements of the Fermi surface topology of $NbTe_2$ and $TaTe_2$ have never been reported. In order to shed light on the origin of the CDW phase and the domain formation observed in these compounds, we have measured the Fermi surface via full-hemispherical angle-resolved photoelectron spectroscopy (ARPES). Scanning tunneling spectroscopy (STS) experiments complement the ARPES data. We suggest that the distortion and the accompanying domain formation is intimately related to the Fermi surface topology. Quantitative assessments of its nesting tendencies are obtained from first-principles band-structure calculations. A computation of the vibrational spectrum and a soft mode analysis support our conclusions.

In the following, we concentrate on $NbTe_2$. Similarities and differences between $NbTe_2$ and $TaTe_2$, especially the absence of superconductivity in $TaTe_2$, will be addressed at the end.

II. EXPERIMENT AND CALCULATION

Full hemispherical ARPES experiments were performed in a modified Vacuum Generator ESCALAB Mark II spectrometer with a residual gas pressure of 2×10^{-11} mbar equipped with a Mg K_α ($h\nu = 1253.6$ eV) x-ray anode, a monochromatized He discharge lamp providing He $I\alpha$ ($h\nu = 21.2$ eV) radiation,[25] and a three channeltron hemispherical electrostatic analyzer kept fixed in space during measurements. The sample is mounted on a manipulator with two motorized and computer controlled rotational axes and may be cooled via a closed cycle refrigerator. Energy resolution is 50 meV, the combined angular resolution of sample manipulator and analyzer is approximately 1°. Surface cleanness and quality before and after ARPES measurements was monitored by x-ray photoelectron spectroscopy (XPS) and checked with low-energy electron diffraction (LEED), respectively. Orientation of the sample was achieved by x-ray photoelectron diffraction (XPD).[26,27]

Scanning tunneling microscopy (STM) and spectroscopy (STS) experiments were carried out with Pt/Ir tips using an Omicron LT-STM in a separate UHV system with a base pressure of 3×10^{-11} mbar. Pure $NbTe_2$ samples were prepared by the standard flux growing techniques. Sample cleavage was carried out in UHV using adhesive tape.

First-principles calculations were performed in the framework of density functional theory (DFT) using the full potential augmented plane wave plus local orbitals (APW+lo) method in conjunction with the generalized gradient approximation (GGA) in the parametrization of Perdew, Burke, and Ernzerhof[28] as implemented in the WIEN2K software package[29] as well as the ABINIT code[30,31] using the local density approximation (LDA) and relativistic separable dual-space Gaussian pseudopotentials[32] for both Nb and Te, taking into account the Nb semicore states.

A recent extension to WIEN2K based on the OPTICS package allows the computation of the frequency dependent ran-
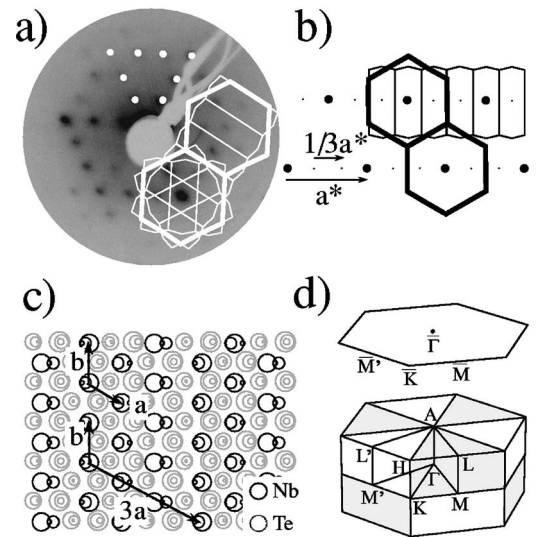

FIG. 2. (a) LEED pattern (75 eV) of $NbTe_2$ at room temperature. (b) Schematic illustration of a single domain (3×1) superstructure as observed in reciprocal space. The fat dots indicate the Γ points of the undistorted trigonal lattice. Due to the (3×1) distortion in real space, two additional spots appear in between these main reflections represented by the small dots. Their spacing is $\frac{1}{3}a^*$. The bold hexagons outline the surface Brillouin zone of the trigonal (1×1) structure. The thin compressed hexagons show the surface Brillouin zone of the (3×1) superlattice. (c) Projection onto the basal plane of the first three Te-Nb-Te sandwiches of the monoclinic structure. The size of the circles is proportional to the z-coordinate. The lattice vectors of the trigonal (1×1) and (3×1) cells are indicated. (d) Bulk and surface Brillouin zone for $1T$-$NbTe_2$ with high symmetry points.

dom phase approximation (RPA) susceptibility.[33] The phonon dispersion is computed with the help of the linear response or density functional perturbation theory (DFPT) capabilities of ABINIT.[34,35] Computational details are given in Ref. 36.

III. RESULTS AND DISCUSSION

A. (3×1) surface superstructure

Transmission electron microscope (TEM) images of $NbTe_2$ show a complicated domain structure (see Ref. 7). Although the crystal structure within the domains is known, insights into the domain structure can be obtained from LEED experiments. Figure 2(a) presents a LEED measurement taken with electrons accelerated to a kinetic energy of 75.0 eV. An interpretation based on the monoclinic reciprocal lattice is not straightforward. The experimental pattern is most easily understood by considering the undistorted trigonal parent structure. Since LEED patterns exhibit Bragg reflections of the 2D surface lattice, the surface Brillouin zone borders are superimposed. The bold hexagons correspond to the surface Brillouin zone of the trigonal (1×1) structure. Due to the monoclinic distortion of the lattice, two additional spots in between the main reflections are visible, which can be understood in terms of a (3×1) superstructure. A sche-

matic illustration is given in Fig. 2(b). The presence of this superstructure results in a new surface Brillouin zone shown in Fig. 2(b). The LEED pattern results from the superposition of three orientational variants, rotated by 120° with respect to each other, of such surface superstructures. Note that a (3×3) superstructure would result in additional spots occurring in the center of the triangle outlined by the white dots in Fig. 2(a). A close inspection of the monoclinic structure in Fig. 2(c) reveals a (3×1) surface unit cell, confirming the experimental finding. The presence of additional spots was already reported earlier[37] and correctly interpreted as a superposition of patterns from three domains. However, the appearance of these superspots has not been recognized as a (3×1) surface superstructure. For completeness, we note that the bulk structure exhibits a $(3 \times 1 \times 3)$ supercell structure, since successive layers are shifted within the plane (see Fig. 1).

The diffuse nature of the LEED pattern has been explained in terms of thermal disorder.[37] Our LEED measurements at low temperature remain diffuse. The presence of a fine domain structure might be responsible for the broadening of the reflections. The average domain size is obtained by comparison of the width of the reflections with the inter-reflection distance. From the measurement in Fig. 2(a) with an average peak width of 0.2 Å^{-1}, we estimate the average domain size to be of the order of 32 Å, which agrees quite well with the domain size from a sample from the same batch observed by STM (see below).

LEED is not able to distinguish between three or six orientational variants of the (3×1) superstructure. Whereas LEED probes the periodicity of the surface, XPD indicates the symmetry of the local environment of the emitting atom. The Te $3d_{5/2}$ XPD diffractogram (not shown) exhibits a threefold symmetry, which clearly shows that only three and not six orientational variants are present, since the presence of domains rotated by 180° would result in a sixfold symmetry. We observed further that XPD diffractograms from different cleavage planes were rotated by 180° with respect to each other, retaining, however, their threefold symmetry, indicating a change in the stacking sequence between successive Te-Nb-Te layers. The presence of the (3×1) superstructure implies a reconstruction of the Brillouin zone. In ARPES experiments, we may thus expect to observe the opening of a gap at the new Brillouin zone border accompanied by a backfolding of bands.

B. Fermi surface topology

Figure 3 presents Fermi surface maps (FSMs) of NbTe$_2$ measured at room temperature, i.e., the intensity distribution for electrons from the Fermi level (E_F). These maps bear in many respects a close resemblance to the FSM's of isopolytopic TaS$_2$ and TaSe$_2$,[18] although in these materials, the CDW distortion is of the $(\sqrt{13} \times \sqrt{13})$ type. Figure 3(a) gives experimental raw data without any further treatment. Near normal emission, high intensity is measured which falls off rather quickly towards larger polar angles. A similar behavior is observed for 1T-TaS$_2$ and 1T-TaSe$_2$ and has been attributed to the d_{z^2} character of the transition metal band. A nor-
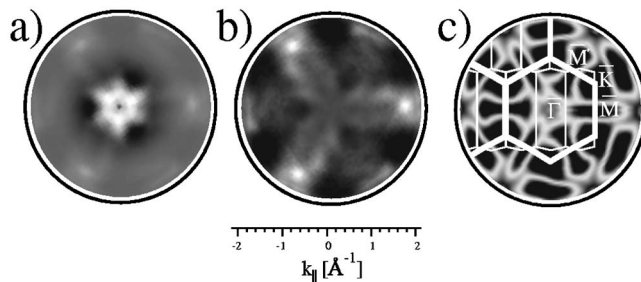

FIG. 3. (a) Angular distribution of electrons from E_F mapped as a function of $\mathbf{k}_\parallel$ at room temperature, white and black correspond to high and low intensity, respectively. (b) Symmetrized and flattened data of (a). (c) Theoretical APW+lo Fermi surface contours for the undistorted trigonal NbTe$_2$ in the free electron final state approximation (Ref. 16) with photon energy $h\nu$=21.2 eV, workfunction ϕ=4 eV and an assumed inner potential V_0=13 eV. Brillouin zones of the (1×1) and one particular orientation of the (3×1) lattice are superimposed.

malization of the FSM by the mean intensity for each polar emission angle as shown in Fig. 3(b) eliminates this dependence and allows one to reveal weaker off-normal features. Centered circular features are then suppressed.

The washed out character of the experimental FSM contours is another common feature of the 1T family. Since the width in $\mathbf{k}_\parallel$ of the bands is independent of temperature, we discharge thermally populated phonons as the origin of the broadening. From the monoclinic distortion it is expected, that the d_{z^2} band, which is mainly responsible for the spectral weight observed at the Fermi energy, splits into several subbands. This results in a larger width of the observed band in energy and consequently also in momentum. Secondly, in the presence of the domain structure, the coherence length of Bloch electrons must be of the order of the average domain size, since electrons get scattered at the domain boundaries. As in LEED, this should lead to a broadening of the crystal momentum of about 0.2 Å^{-1}, consistent with the broadening observed in the experimental FSM.

Great care is required in determining the Fermi surface crossings from the experimental data. Due to the weak dispersion and $\mathbf{k}$-dependent photoemission matrix elements, which lead to intensity variations which have nothing to do with Fermi crossings, an unambiguous extraction of the Fermi surface needs additional information. We have measured the energy dispersion of the NbTe$_2$ d_{z^2} band along $\bar{\Gamma}\bar{M}$ [Fig. 4(a)], $\bar{\Gamma}\bar{M}'$, and $\bar{\Gamma}\bar{K}$ at room temperature and at $T < 20$ K (not shown). The band topology is not affected by this change in temperature indicating the absence of a phase transition in this temperature range. In order to determine the location of Fermi crossings, we applied the symmetrization method described in Ref. 38. No quasiparticle crossing has been found for any of the measured energy dispersion curves. Thus, strictly speaking, the maps in Fig. 3 are not Fermi surfaces. The observed intensity originates from bands which come close to the Fermi level, but must not be associated with quasiparticle crossings, but rather spectral weight which leaks across the Fermi level. The signature of such a pseudogapped Fermi surface is also observed in TaS$_2$ and
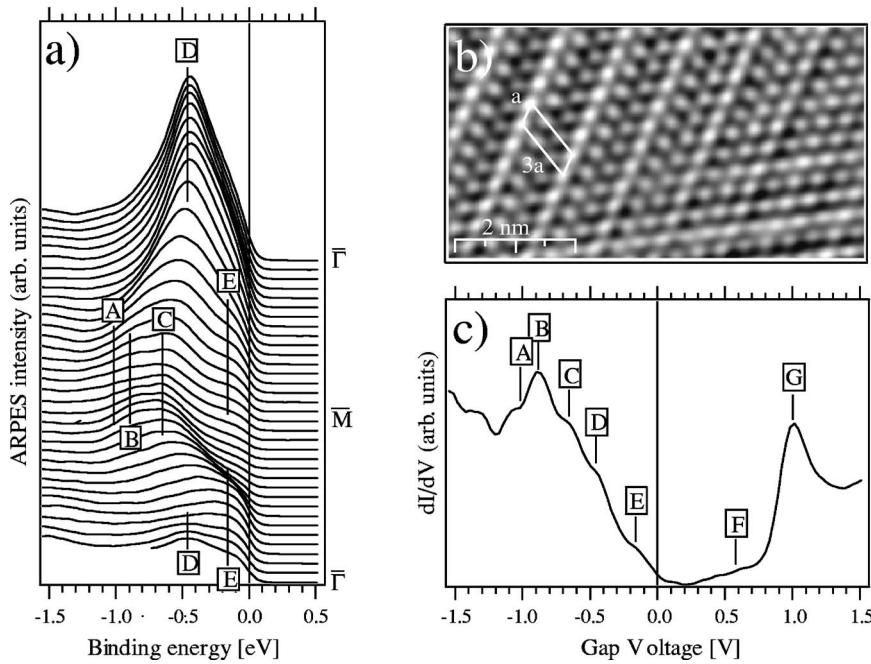
FIG. 4. Comparison between ARPES and STS data. (a) Room temperature ARPES spectra along $\bar{\Gamma}\bar{M}$. (b) STM topography of the (3×1) phase of NbTe$_2$ at 77 K (V=3 mV, I=2.9 nA). (c) STS spectrum at 77 K measured with a lock-in amplifier, modulation frequency 1 kHz, modulation amplitude 30 mV. The sample-tip distance was chosen in order to have a tunneling current of 0.8 nA for a bias voltage of −1.5 V.

TaSe$_2$ (Ref. 18) as well as in high-T_c superconductors[39] and has remained a controversial topic.

Comparison of the experimental data with the theoretical DFT Fermi surface map shown in Fig. 3(c) for the undistorted trigonal structure shows that the symmetry of the undistorted Fermi surface is clearly dominant. In contrast to the superspots in LEED data, no clear evidence for the superstructure in the form of additional backfolded features is apparent. Voit *et al.*[40] have argued that in the presence of a weak superimposed periodic potential, the spectral weight remains on the unperturbed bands. An additional potential due to the (3×1) superstructure manifests itself through the opening of small gaps localized at the new Brillouin zone borders. In the presence of three domains, details of such a gap structure are buried below the bands of the other two domains, which do not experience the potential in this direction, and unfortunately it is impossible to deconvolute the contributions from the various domains.

It should be noted that DFT for the undistorted compound predicts a truly metallic Fermi surface, whereas our experimental ARPES data of the distorted structure does not display any quasiparticle crossings. This indicates that the transition from the high symmetry structure to the monoclinic structure is driven by a gain in electronic energy all over the Brillouin zone. The removal of the entire Fermi surface is not consistent with an explanation based solely on a 2D Peierls scenario.

Additional information on the occupied and empty state electronic structure of NbTe$_2$ is obtained via STM. The chain like structure observed by STM within the domains [Fig. 4(b)] is a consequence of the anisotropy of the (3×1) lattice and indicates a possible nesting scenario as the origin of the distortion (see later). For comparison between tunneling and photoemission spectra, we have pasted the peak positions determined from the STS spectrum Fig. 4(c) onto the ARPES spectra Fig. 4(a). Although it is difficult to tell, which part of k space is sampled by STS, features A, B, C, D, and E can be

clearly identified with their counterpart in the ARPES data. As already concluded from ARPES data, the STS spectrum does not exhibit a clear gap at the Fermi level. In the pseudogapped region between feature E and G, several small peak shoulders such as F are observed, indicating a finite density of states. The theoretical band structure discussed in the next section will allow further interpretation of these data.

The absence of any clear quasiparticle crossing stands in contradiction with the metallic character of the resistivity vs temperature curves[9] and can, as discussed above, not be explained by only taking into account the Peierls scenario. Electron-phonon coupling is expected to be relatively strong for the tellurides,[6] consequently polaronic effects may play a role. Polarons recently received increased attention for the interpretation of anomalously broad ARPES features.[41–43] Within the Fermi-liquid picture, ARPES peaks are attributed to quasiparticle excitations, whose lifetime increases when approaching the Fermi level. This procedure is well justified by recent theoretical calculations of the spectral function for the spinless Holstein model in the weak coupling regime.[44,45] In contrast in the strong coupling regime, the coherent quasiparticle band flattens considerably and possesses exponentially small spectral weight.[44,45] Most spectral weight is transferred to a broad incoherent part on the high-energy side. Whereas the center of mass or first moment of the spectral function remains unaffected by the electron-phonon interaction at low band-fillings, it experiences a rigid shift proportional to the polaron binding energy at higher fillings.[46] A polaronic scenario would thus allow to explain the apparent absence of quasiparticle crossings as well as the broadened line shape in the experimental ARPES spectra of NbTe$_2$. However, an ideal experimental model system suited for ARPES measurements, for which the theoretical predictions for polaronic spectral signatures can be verified, still has to be found.
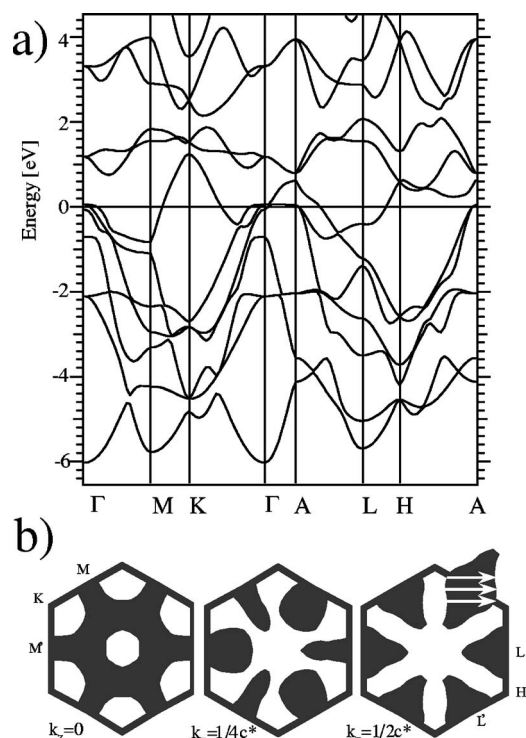
FIG. 5. (a) APW+lo band structure along high symmetry directions for 1T-NbTe$_2$. (b) Cuts through the Fermi surface at $k_z=0$, $k_z=c^*/4$, $k_z=c^*/2$. Nesting vectors of length $q=1/3a^*$ are indicated.

C. Electronic band structure

Comparing NbTe$_2$ and TaTe$_2$ to their homologues in the sulfide and selenide family, such as TaS$_2$, TaSe$_2$, NbS$_2$, and NbSe$_2$, it is tempting to interpret the monoclinic distortion in terms of a CDW phase. The existence of such a phase requires electron-phonon communication in the undistorted compound. Trigonal 1T-NbTe$_2$ is not available for experiment. In order to make some progress, we investigated the electronic structure of the undistorted crystal in the framework of DFT (see Appendix for structural details).

In Fig. 5(a) we show the band structure of 1T-NbTe$_2$ along high symmetry directions obtained with the APW+lo basis set. The positions of the high symmetry points in the Brillouin zone are indicated in Fig. 2(d). The overall agreement with the bandstructure obtained using the pseudopotential method (not shown) is very good. Slight variations can be attributed to the different exchange-correlation functional and convergence parameters.

From a simple ionic picture, one would expect the Nb^{4+} ions to have only one remaining d electron, resulting in a half-filled band crossing the Fermi level, while the six Te 5p bands from the two Te atoms are fully occupied. Obviously this picture neglects all other bonding effects, since an appreciable admixture of Nb 4d states exists in the Te p bands, indicating covalent interactions and less ionic bonding. Integration of the partial charges inside the muffin tin sphere of the respective atom allows to identify the character of the different bands and correctly reproduces this coarse prediction. The first four empty bands above the Fermi level are the remaining four Nb 4d bands.

Due to the octahedral coordination of the Nb atoms between the Te atoms and the resulting crystal field, the five Nb d bands are split into a lower triplet of t_{2g} states and an upper doublet of e_g states separated by a small gap at 2 eV binding energy. The σ bonding e_g orbitals have higher energies because they interact strongly with the neighboring Te atoms. The orbital degeneracy of the octahedral t_{2g} manifold is reduced in a Jahn-Teller-like fashion by a trigonal elongation of the Te octahedra along the c axis.

The $P\bar{3}m1$ space group contains an unique z axis perpendicular to the layers of the crystal. Further insights can be obtained by dividing the d orbitals into (a) d_{z^2} (out-of-plane orientation), (b) $d_{x^2-y^2}$, d_{xy} (in-plane orientation), and (c) d_{xz}, d_{yz}. The half-filled, lowest-lying t_{2g} band, which crosses the Fermi level, has mainly Nb d_{z^2} character, whereas the remaining two bands of the t_{2g} manifold (first two unoccupied bands) exhibit dominant Nb $d_{x^2-y^2}$ and d_{xy} character. While these in-plane d orbitals do not interact strongly with the Te p orbitals, the d_{z^2} orbitals, due to their orientation towards the Te layers, are more strongly hybridized with the Te orbitals especially around the Brillouin zone center. This orbital resonance might be at the origin of the buckling of the Te atoms. Whereas the formation of "trimers" by the Nb atoms is consistent with a Peierls scenario, the buckling of the Te layer rather points towards a band Jahn-Teller distortion.[47] However, inspection of Fig. 1 shows, that the Te atoms of type c which fall in between the Nb "trimers" are shifted towards the Nb layer, whereas the other two Te atoms, labeled a and b, remain approximately at the original distance. Since the "trimerization" of the Nb atoms reduces the overlap between the Te atoms of type c and its neighboring Nb atoms, these Te atoms approach the Nb layer to recover the overlap.

We now compare the theoretical bandstructure for the undistorted structure with ARPES and STS data in Fig. 4 from the distorted crystal. We identify feature G on the unoccupied side of the STS spectrum with the t_{2g} doublet which disperses around 1 eV. These empty bands appear to be only weakly affected by the reduction of the symmetry towards the monoclinic space group. Due to the hybridization of the d_{z^2} band with the Te p bands and the modification of the bandstructure induced by the distortion to the monoclinic structure, an identification of the features in the occupied part of the spectrum is not so straightforward. The theoretical dispersion along ΓM is qualitatively in agreement with the ARPES data, where most bands have the tendency to disperse towards higher binding energies when going from $\bar{\Gamma}$ to $\bar{M}$. However, whereas the Nb d_{z^2} band clearly crosses the Fermi level in the theoretical bandstructure, no such crossing is observed in our experimental results. This indicates that the distortion to the monoclinic structure has profound effects on the Nb d_{z^2} band.

We also computed the bandstructure of NbTe$_2$ in the monoclinic structure (not shown). The distortion reduces the density of states at the Fermi level approximately by a factor of 2. However, the pseudogap observed above the Fermi level in the STS spectrum (Fig. 4) is not reproduced by theory, since a considerable amount of states is located in this region. This discrepancy is possibly caused by polaronic

effects as discussed above. Furthermore localization of the electrons decreases the bandwidth W of the d_{z^2} band and consequently the crucial parameter W/U with U the on-site Coulomb repulsion energy. This opens up the possibility of increased correlation effects. Mott scenarios have been suggested for $1T$-TaS_2 (Ref. 48) and $1T$-$TaSe_2$.[23] However, instead of trying to explain the discrepancy between experiment and theory with the insufficient treatment of correlation effects within LDA or GGA, we wish to point out that the disagreement between theory and experiment may be caused by the theoretical treatment of the distorted structure within DFT or more generally within the Bloch theory of periodic crystals. Since the monoclinic cell contains 18 inequivalent atom positions, we obtain six times more bands than for the band-structure calculated for the trigonal unit cell. The huge amount of bands renders the comparison with the experimental data difficult. In several studies on distorted compounds, we noticed that the spectral weight observed in ARPES experiments tends to exhibit the symmetry of the undistorted structure and that backfolded features carry generally only a small amount of spectral weight. The rigorous backfolding of bands within the theoretical description does not appear to apply to real systems. A first step towards a theoretical framework taking into account this observation has been taken by Voit *et al.*,[40] who weights the eigenvalues of the distorted structure obtained from a simple tight-binding model by the projection of the corresponding eigenvectors onto the eigenvectors of the undistorted structure. For comparison between theoretical and experimental data, it would be clearly desirable to implement an equivalent scheme into *ab initio* codes.

When two portions of the Fermi surface are flat and parallel, nesting occurs, and the susceptibility diverges logarithmically. In the isotropic electron gas, favorable nesting conditions are only encountered in one dimension, where the Fermi surface consists of two points. However, materials with an anisotropic Fermi surfaces may exhibit regions where scattering becomes more singular than in the isotropic electron gas. The presence of the (3×1) superstructure in the monoclinically deformed structure would then imply a nesting vector $\mathbf{q} = \frac{1}{3}\mathbf{a}^*$. Figure 5(b) presents three horizontal cross sections through the Fermi surface of $1T$-$NbTe_2$ for $k_z = |\mathbf{k}_\perp| = 0$, $\frac{1}{4}c^*$, and $\frac{1}{2}c^*$. The black areas indicate occupied, the white areas unoccupied states of the Nb d_{z^2} band. Based on a Fermi surface obtained by extrapolation from the calculated results for the $1T$ sulphides and selenides, Wilson[6] already noted that a wave vector of $\mathbf{q} = \frac{1}{3}\mathbf{a}^*$ is too large for nesting across M and M′. However, since $NbTe_2$ is not an ideal 2D crystal, nesting becomes possible across L and L′ as shown in Fig. 5(b). The arrows indicate one family of the three symmetry-related experimental Fermi surface nesting vectors $\mathbf{q} = \frac{1}{3}\mathbf{a}^*$. Furthermore the nested areas are relatively large encouraging a Fermi surface nesting scenario. Obviously, the contributions from different nesting vectors to the static susceptibility are hard to estimate on the basis of Fermi surface cross sections. In order to obtain quantitative confirmation for the $\mathbf{q} = \frac{1}{3}\mathbf{a}^*$ nesting vector, we integrated the DFT band structure to obtain the susceptibility for all vectors within the Brillouin zone.
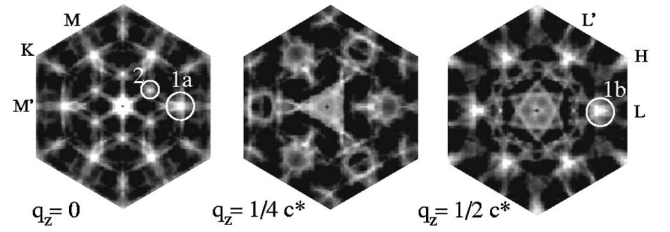

FIG. 6. RPA susceptibility in the first Brillouin zone at $q_z = 0$ (ΓMK plane), $\frac{1}{4}c^*$ and $\frac{1}{2}c^*$ (ALH plane) obtained by integration of the APW+lo Fermi surface of Fig. 5(b). The peaks marked 1a and 1b occur exactly at $q_x = \frac{1}{3}a^*$. Feature 2 is close to the nesting vector of the $\sqrt{19} \times \sqrt{19}$ CDW phase.

D. RPA susceptibility

For the computation of the static susceptibility, the following expression has been used:[49]

$$\chi(\mathbf{q}) = \sum_{n',n,\mathbf{k}} \delta(\epsilon_{n',\mathbf{k}+\mathbf{q}} - \epsilon_{n,\mathbf{k}}). \tag{1}$$

The Dirac δ gives a contribution of either 1 or 0 depending on whether $\mathbf{q}$ is a nesting vector or not. Matrix elements are neglected, thus all electron-hole pairs are treated on an equal basis.

The results of our calculation are presented as linear gray scale plots in Fig. 6 with white indicating a large response of the electron system. Strong nesting is present for small, but nonvanishing $\mathbf{q}$ vectors. These contributions are due to intra-band contributions from weakly dispersing bands and can be reduced by choosing a smaller energy window.

Highly interesting is the peak at $\mathbf{q} = \frac{1}{3}\mathbf{a}^*$ along the ΓM and $\Gamma M'$ directions in Fig. 6 (feature 1a). We associate this peak with a nesting vector leading to the (3×1) superstructure observed by LEED. Thus, the electronic structure of trigonal $NbTe_2$ appears unstable with respect to a potential with wave vector $\mathbf{q} = \frac{1}{3}\mathbf{a}^*$. The peak is not confined to the ΓMK plane, but is smeared out along q_z, thus allowing an out-of-plane component for the nesting vector. A second maximum (feature 1b) with the same in-plane coordinates is seen along the AL and AL' direction. We wish to draw attention to the fact that the nesting vector sketched in the ALH plane of Fig. 5(b) corresponds to feature 1a, which lies in the basal plane, whereas feature 1b connects parts of the Fermi surface with different k_z. Our calculation, however, does not reproduce a single peak at $\mathbf{q} = \frac{1}{3}\mathbf{a}^* + \frac{1}{3}\mathbf{c}^*$, which would be required to explain the occurrence of the $(3 \times 1 \times 3)$ superstructure. At present, it is unclear, if the shift between successive layers is directly induced by the nesting scenario or a consequence of it. According to the calculation, nesting takes place in the Nb d_{z^2} band and since the Nb atoms are screened by the surrounding Te layers, we may assume that the nesting mechanism operates in each individual Te-Nb-Te sandwich independently. As a consequence one might argue that the resulting CDW adjusts its phase in each sandwich, so as to minimize the repulsive intersandwich interaction and to maximize the attractive intrasandwich energy. Inspection of Fig. 1 shows, that the Te atoms closest to the Nb layer, type

c, falls approximately in between the two Te atoms, type a and b, of the next sandwich which are further away from the Nb atoms. This maximizes the distance between individual Te "anions" of successive Te-Nb-Te sandwiches and increases the overlap with the Nb "cations." In this framework, the tripling of the unit cell perpendicular to the layers is a consequence of the in-plane (3×1) reconstruction associated with feature 1a, which in turn is triggered by Fermi surface nesting. This would also explain, why we do not observe a $(3 \times 1 \times 2)$ reconstruction associated with feature 1b, since such a configuration does not minimize the inter-sandwich interaction. A triple-axis distortion as in TaS$_2$,[48,50] in which surrounding metal atoms are shifted radially and within the plane towards a central metal atom to form a contracted star (see Ref. 16 for a sketch[17,18]), is reserved to clusters of $6n+1$ metal atoms, where n is the number of shells surrounding the central atom. This leads to a very precise condition on the nesting vector $\mathbf{q}=1/\sqrt{6n+1}\mathbf{a}^*$. Since the Fermi surface of NbTe$_2$ exhibits dominant nesting at $\mathbf{q}=\frac{1}{3}\mathbf{a}^*$, such a scenario is excluded, and the crystal locally selects one of the directions, which leads to the chainlike (3×1) distortion and the breakup into domains.

A second maximum (feature 2) at $q=0.19a^*$ along ΓK might account for the starlike $(\sqrt{19} \times \sqrt{19})$ CDW phase, where three shells $(n=3)$, each containing six metal atoms, are shifted towards a central atom, although it is slightly displaced from the ideal value $q=1/\sqrt{19}a^*=0.23a^*$. This nesting vector leads to an incommensurate phase, which was observed after cooling of heat-pulsed crystals to a temperature just above room temperature.[6] Our $q=0.19a^*$ agrees with Wilson's proposal for nesting across the M and M′ points. The absence of an out-of-plane component of this nesting vector in our calculation is confirmed by experiment.[6] Upon cooling to room temperature, the $(\sqrt{19} \times \sqrt{19})$ CDW rotates away from ΓK by 6.6° (Ref. 6) to become commensurate with the parent lattice. Such a second-order incommensurate-to-commensurate (lock-in) phase transition has been modelled theoretically via a Landau free energy expansion,[51] describing the competition of the terms that determine the individual periodicities and the term that promotes commensurability via gap formation. A similar scenario is followed by the $(\sqrt{13} \times \sqrt{13})$ CDW of 1T-TaS$_2$, where in contrast to NbTe$_2$ the nesting vector points along ΓM.

E. Phonon band structure

The occurance of a maximum in the electron susceptibility alone does not explain the distortion to the monoclinic structure. The presence of a perturbation with the corresponding $\mathbf{q}$ vector is necessary. In the one-dimensional Peierls scenario this potential is provided by a soft phonon mode.

The DFPT phonon band structure for the relaxed trigonal NbTe$_2$ structure obtained by diagonalization of the dynamical matrix along high symmetry lines is shown in Fig. 7. The lowest lying acoustic branch exhibits imaginary frequencies. DFPT contains the implicit assumption that phonons are simple harmonic modes. Soft modes are by definition anhar-
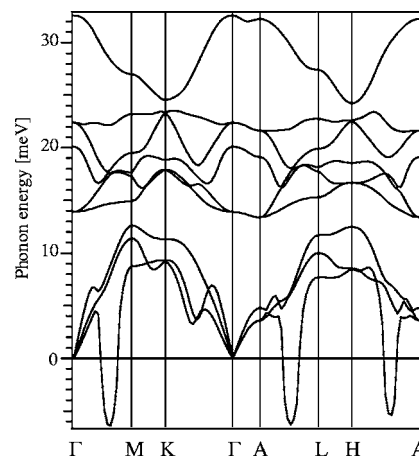

FIG. 7. Phonon dispersion of 1T-NbTe$_2$ along high symmetry lines obtained by the response function capabilities of ABINIT. Frequencies below 0 meV are imaginary. All free degrees within the trigonal $P\bar{3}m1$ space group were relaxed using the Broyden-Fletcher-Goldfarb-Shanno minimization scheme as implemented in the ABINIT code. The optimized LDA lattice parameters underestimate the values derived from Brown's experimental values (Ref. 3) for the trigonal structure by less then 1%, following the general trend observed for LDA results (Ref. 55). The LDA equilibrium value for $z_{red}=0.274$ is also in good agreement with the derived averaged value $z_{red}=0.277$ (see the Appendix).

monic and their frequency goes to zero. Zero frequency implies that the lattice structure is unstable and will transform, typically, to a lower symmetry phase. In the extreme case, electronic structure calculations may give an imaginary phonon frequency indicating that the ideal structure is unstable.[52] The phonon frequencies are the square roots of the eigenvalues of the dynamical matrix. Imaginary frequencies correspond to negative eigenvalues of the dynamical matrix. A negative entry in the diagonalized dynamical matrix contributes a negative energy to the total Hamiltonian, indicating that the expansion was not carried out around the equilibrium configuration. Thus there exists an energetically more favorable configuration. At high temperature, the lattice has sufficient energy to overcome the energy barrier between two or more symmetry-related variants of the low-temperature structure such that the average observed structure has higher symmetry. In such cases the ideal structure is stabilized by high temperature and will undergo a phase transition on cooling, to a low-temperature phase whose symmetry differs by the symmetry of the imaginary mode. The most unstable modes in Fig. 7 occur along $\mathbf{q}=(1/3,0,q_z)a^*$. This strongly supports the Fermi surface nesting scenario for NbTe$_2$. Furthermore, from an analysis of the eigenvectors of the dynamical matrix, the distorted structure may be qualitatively constructed. The Nb atoms oscillate predominantly within the basal plane, the Te atoms have a dominant out of plane component, which is of opposite sign for the two inequivalent Te atoms.

The Raman spectrum of the monoclinic NbTe$_2$ has been measured by Erdogan and Kirby[53] at $T=80$, 300, and 420 K. No phase transition was observed in this temperature range. They identified 11 peaks in their spectra (see Table I), instead

TABLE I. Experimental (Ref. 53) and theoretical Raman modes in meV. Experimental resolution 0.5 meV. The theoretical optical modes at the Brillouin zone center are labeled by their corresponding irreducible representation obtained from a symmetry analysis carried out by ABINIT. Only the even modes (subscript g) are Raman active. The subscript u labels IR active odd modes. For comparison with experiment we also list the LDA energies of the modes at $\mathbf{q} = \frac{1}{3}\mathbf{a}*$ which are expected to lie on the new Brillouin zone center of the distorted structure.

Experiment (Ref. 53)	LDA $\mathbf{q}=0$	back-folded LDA $\mathbf{q}=(0.34,0,0)a^*$
6.9		6.4[a]
8.7		8.8
10.4		9.7
13.0	13.9 (E_g)	
13.6		14.7
16.2		17.5, 17.6
18.5		17.9
19.6	20.1 (A_{1g})	
21.0	22.4 (E_u)	22.2
27.2		28.3
31.5	32.6 (A_{1u})	

[a]Linearly interpolated between 4.5 meV at $\mathbf{q}=0.2a^*$ and 8.8 meV at $\mathbf{q}=0.5a^*$.

of the two Raman active modes predicted by group theory for the undistorted compound. Thus unlike in ARPES measurements, where the unreconstructed (1×1) structure dominates, phonon bands get backfolded.

A comparison between the experimental Raman peaks and the LDA results is shown in Table I. From a strictly two-dimensional point of view neglecting interlayer effects, $\mathbf{q} = \frac{1}{3}\mathbf{a}^*$ modes are expected to lie at the new Brillouin zone center. For comparison with the experimental data, these modes are included in Table I. A low intensity mode was measured at 31.5 meV and may be identified with the $\mathbf{q}=0$ mode at 32.6 meV. The low intensity appears to be reminiscent of its IR character in the undistorted structure. A second peak is found in the experimental spectrum at 27.2 meV and may correspond to the backfolded 28.3 meV mode at $\mathbf{q} = \frac{1}{3}\mathbf{a}^*$. Nine experimental peaks are found in the range between 6.9 to 21 meV and correspond to the backfolded acoustic and low-lying optical bands. Including backfolded LDA modes from $\mathbf{q} = \frac{1}{3}\mathbf{a}^*$, *ab initio* results indicate the presence of a maximum of 10 modes in the range between 8.8 and 22.4 meV. An additional, even lower lying acoustic mode is expected due to the stabilization of the unstable high symmetry mode within the monoclinic structure. With a rms of relative deviation of 5.8% between experiment and LDA, the quantitative agreement can be qualified as fairly good.[54] However, not all the LDA modes are expected to be Raman active. Experimental data for the IR modes are not available in the literature.

IV. COMPARISON WITH TaTe₂

In this article we have concentrated on NbTe₂. We want to stress, however, that most of our conclusions appear to be valid as well for the isostructural TaTe₂. Our experimental LEED and ARPES data of TaTe₂ show a very similar behavior. Furthermore the electronic band structure for trigonal TaTe₂ differs only slightly from the one obtained for NbTe₂. We thus conclude that the nesting behavior of the Fermi surface for TaTe₂ is the same as for NbTe₂. However, TaTe₂ in contrast to NbTe₂ does not become superconducting at low temperature.

Differences between the two compounds are expected in the vibrational dynamics, since the phonon frequencies scale as the inverse square root of the mass of the oscillating atoms. The acoustic branches of the phonon band structure for trigonal TaTe₂, however, exhibit a very similar topology as for NbTe₂ with unstable modes along $\mathbf{q}=(1/3,0,q_z)a^*$ in the lowest lying branch. In contrast the bands of the optical manifold are drastically rearranged. The energy at Γ of the highest lying A_{1u} mode is reduced to 27.6 meV for TaTe₂ (32.6 meV for NbTe₂). The E_u mode changes from 22.4 meV for NbTe₂ to 19.0 meV for TaTe₂ and comes to lie between the two even modes E_g and A_{1g}, whose energies at Γ fall within less than 1 meV onto the energies of the NbTe₂ branches. It is interesting to note that the odd (subscript u) IR modes include Nb/Ta atom motion, whereas for the even (subscript g) Raman modes the Nb/Ta atoms are at rest. This correlates well with the rescaling of the odd branches and the invariance of the even branches upon substitution of Nb by the heavier Ta atoms. These differences in the vibrational spectrum of the two compounds might possibly explain why TaTe₂ is not superconducting, whereas NbTe₂ becomes superconducting below $T=0.5-0.74$ K.

V. SUMMARY AND CONCLUSION

We investigated the origins of the CDW phases of NbTe₂. LEED experiments revealed the presence of three coexisting domains exhibiting a (3×1) superstructure, consistent with the structure derived from x-ray diffraction data and TEM and STM images. We carried out a detailed *ab initio* study of the nesting properties of the Fermi surface of the undistorted compound and found a singularity in the RPA susceptibility at $\mathbf{q} = \frac{1}{3}\mathbf{a}^*$. In order to consolidate the absence of an out-of-plane component of this theoretical nesting vector with the actual $(3 \times 1 \times 3)$ structure, we suggest that the CDW within each individual Te-Nb-Te sandwich adjusts its phase, so as to minimize the repulsive intersandwich interaction (by maximizing the distance between Te "anions" of successive sandwiches) and to maximize the intrasandwich interaction (by maximizing the overlap of the Te orbitals with their neighboring Nb orbitals). A second peak at $q \approx (1/\sqrt{19})a^*$ along ΓK accounts for the $(\sqrt{19} \times \sqrt{19})$ CDW phase observed by TEM on heat pulsed crystals. *Ab initio* phonon calculations and a soft mode analysis support the Fermi surface nesting scenario.

Using angle-resolved photoemission in the Fermi surface mapping mode at room temperature and at $T<20$ K, we found no quasiparticle crossings in the (3×1) CDW phase of NbTe₂. No phase transition was observed within this temperature range. Localized gaps at the Fermi level expected for the nesting scenario could not be observed, since the

photoelectron signal is a superposition of three domains. Instead our ARPES spectra indicate a pseudogaplike signature over the entire sampled portion of the Brillouin zone, which can not be understood by considering only the Peierls scenario and is not reproduced by DFT. The angular distribution of the spectral weight observed at the Fermi level is dominated by the residual (1×1) symmetry and resembles the metallic DFT Fermi surface of the undistorted compound. STS spectra indicate that the unoccupied bands are only weakly affected by the distortion towards the monoclinic structure, whereas most spectral weight of the Nb d_{z^2} band is transferred to states below the Fermi energy. The presence of polarons within the Peierls distorted state possibly accounts for the absence of any apparent quasiparticle crossing and the anomalously broad features observed in the ARPES spectra.

ACKNOWLEDGMENTS

APPENDIX

The structure derived by Brown[3] is given in Table II. As a starting point for theoretical calculations within the undistorted trigonal structure, the average values in Table III have been used. The monoclinic cell parameters, marked with a m subscript are related to the undistorted cell parameters, without subscript, by

$$a_m \approx 3\sqrt{3}a, \quad b_m \approx a, \quad c_m \approx \frac{c}{\sin \beta}. \quad \text{(A1)}$$

For a the value of b_m has been chosen. The value of c has been obtained via Eq. (A1). The average value of the z coordinate for Te was estimated by averaging z_{red} of Te$_1$, Te$_2$, Te$_3$ in the monoclinic structure taking into account a small offset induced by the differences in z_{red} between Nb$_1$ and Nb$_2$ as well as the multiplicity n of each atom:

$$\bar{z}_{red}(\text{Te}) = \frac{1}{N(\text{Te})} \sum_{i=1}^{3} n(\text{Te}_i) z_{red}(\text{Te}_i)$$

$$+ \left(1 - \frac{1}{N(\text{Nb})} \sum_{i=1}^{2} n(\text{Nb}_i) z_{red}(\text{Nb}_i) \right), \quad \text{(A2)}$$

where $N(\text{Nb})=6$ and $N(\text{Te})=12$ is the total number of Nb and Te atoms per unit cell, respectively, and $z_{red}(\text{Nb}_1)=1$.

TABLE II. NbTe$_2$ structure data: $a_m=19.39$ Å, $b_m=3.642$ Å, $c_m=9.375$ Å, $\beta=134.58°$, space group 12 ($C2/m$).[3]

Atoms	Point set	x_{red}	y_{red}	z_{red}
Nb$_1$	2a	0.0000	0.000	0.0000
Nb$_2$	4i	0.6397	0.000	0.9882
Te$_1$	4i	0.6497	0.000	0.2898
Te$_2$	4i	0.2970	0.000	0.2148
Te$_3$	4i	0.9961	0.000	0.3020

TABLE III. Averaged trigonal 1T-NbTe$_2$ structure data: $a=b=b_m=3.642$ Å, $c=6.678$ Å, space group 164 ($P\bar{3}m1$).

Atoms	Point set	x_{red}	y_{red}	z_{red}
Nb	1a	0.0	0.0	0.0
Te	2d	1/3	2/3	0.2767

*Electronic address: corsin.battaglia@unine.ch; URL: http://www.unine.ch/phys/spectro

†Present address: ABB, CH-5600 Lenzburg, Switzerland.

[1] R. Peierls, *Quantum Theory of Solids* (Clarendon, Oxford, 1955).

[2] W. Kohn, Phys. Rev. Lett. **2**, 393 (1959).

[3] B. Brown, J. Appl. Crystallogr. **20**, 264 (1966).

[4] J. van Landuyt, G. van Tendeloo, and S. Amelinckx, Phys. Status Solidi A **26**, 585 (1974).

[5] J. van Landuyt, G. van Tendeloo, and S. Amelinckx, Phys. Status Solidi A **29**, K11 (1975).

[6] J. A. Wilson, Phys. Rev. B **17**, 3880 (1978).

[7] J. Wilson and A. Yoffe, Adv. Phys. **18**, 193 (1969).

[8] L. Brixner, J. Inorg. Nucl. Chem. **24**, 2257 (1962).

[9] S. Nagata, T. Abe, S. Ebisu, Y. Ishihara, and K. Tsutsumi, J. Phys. Chem. Solids **54**, 895 (1993).

[10] A. Vernes, H. Ebert, W. Bensch, W. Heid, and C. Naether, J. Phys.: Condens. Matter **10**, 761 (1998).

[11] M. van Maaren and G. Schaeffer, Phys. Lett. **24A**, 645 (1967).

[12] A. Kidron, Phys. Lett. **24A**, 12 (1967).

[13] T. Pillo, J. Hayoz, H. Berger, M. Grioni, L. Schlapbach, and P. Aebi, Phys. Rev. Lett. **83**, 3494 (1999).

[14] T. Pillo, J. Hayoz, D. Naumović, H. Berger, L. Perfetti, L. Gavioli, A. Taleb-Ibrahimi, L. Schlapbach, and P. Aebi, Phys. Rev. B **64**, 245105 (2001).

[15] T. Pillo, J. Hayoz, H. Berger, R. Fasel, L. Schlapbach, and P. Aebi, Phys. Rev. B **62**, 4277 (2002).

[16] P. Aebi, T. Pillo, H. Berger, and F. Lévy, J. Electron Spectrosc. Relat. Phenom. **117**, 433 (2001).

[17] M. Bovet, S. van Smaalen, H. Berger, R. Gaal, L. Forro, L. Schlapbach, and P. Aebi, Phys. Rev. B **67**, 125105 (2003).

[18] M. Bovet, D. Popović, F. Clerc, C. Koitzsch, U. Probst, E. Bucher, H. Berger, D. Naumović, and P. Aebi, Phys. Rev. B **69**, 125117 (2004).

[19] F. Clerc, M. Bovet, H. Berger, L. Despont, C. Koitzsch, and P. Aebi, Physica B **351**, 245 (2004).

[20] F. Clerc, M. Bovet, H. Berger, L. Despont, O. Gallus, L. Patthey,

M. Shi, J. Krempasky, M. Garnier, and P. Aebi, J. Phys.: Condens. Matter **16**, 3271 (2004).

[21] L. Perfetti, T. A. Gloor, F. Mila, H. Berger, and M. Grioni, Phys. Rev. B **71**, 153101 (2005).

[22] K. Horiba, K. Ono, J. H. Oh, T. Kihara, S. Nakazono, M. Oshima, O. Shiino, H. W. Yeom, A. Kakizaki, and Y. Aiura, Phys. Rev. B **66**, 073106 (2002).

[23] L. Perfetti, A. Georges, S. Florens, S. Biermann, S. Mitrovic, H. Berger, Y. Tomm, H. Höchst, and M. Grioni, Phys. Rev. Lett. **90**, 166401 (2003).

[24] S. Colonna, F. Ronci, A. Cricenti, L. Perfetti, H. Berger, and M. Grioni, Phys. Rev. Lett. **94**, 036405 (2005).

[25] T. Pillo, L. Patthey, E. Boschung, J. Hayoz, P. Aebi, and L. Schlapbach, J. Electron Spectrosc. Relat. Phenom. **97**, 243 (1998).

[26] P. Aebi, R. Fasel, D. Naumović, J. Hayoz, Th. Pillo, M. Bovet, R. G. Agostino, L. Patthey, L. Schlapbach, F. P. Gil, H. Berger, T. J. Kreutz, and J. Osterwalder, Surf. Sci. **402–404**, 614 (1998).

[27] R. Fasel and P. Aebi, Chimia **56**, 566 (2002).

[28] J. P. Perdew, K. Burke, and M. Ernznerhof, Phys. Rev. Lett. **77**, 3865 (1996).

[29] P. Blaha, K. Schwarz, G. Madsen, D. Kvasnicka, and J. Luitz, WIEN2K, *An Augmented Plane Wave + Local Orbitals Program for Calculating Crystal Properties* (Karlheinz Schwarz, Technische Universität Wien, Austria, 2001).

[30] X. Gonze, J.-M. Beuken, R. Caracas, F. Detraux, M. Fuchs, G.-M. Rignanese, L. Sindic, M. Verstaete, G. Zerah, F. Jollet, M. Torrent, A. Roy, M. Mikrami, Ph. Ghosez, J.-Y. Raty, and D. C. Allan, Comput. Mater. Sci. **25**, 478 (2002).

[31] The ABINIT code is a common project of the Université Catholique de Louvain, Corning Incorporated, and other contributors (URL http://www.abinit.org).

[32] C. Hartwigsen, S. Goedecker, and J. Hutter, Phys. Rev. B **58**, 3641 (1998).

[33] C. Ambrosch-Draxl and J. O. Sofo, cond-mat/0402523 (unpublished).

[34] X. Gonze, Phys. Rev. B **55**, 10337 (1997).

[35] X. Gonze and C. Lee, Phys. Rev. B **55**, 10 355 (1997).

[36] In WIEN2K, the APW+lo basis was expanded up to $R_{MT}K_{max}=7$, where K_{max} is the maximum modulus for the reciprocal lattice vector and R_{MT} is the radius of the muffin tin sphere. Inside the muffin tin sphere, the l expansion of the nonspherical potential and charge density is carried out up to $l_{max}=10$. For the trigonal structure, k-integration over the Brillouin zone is performed using 2000 k points. For the computation of the static susceptibility, integration over the Brillouin zone has been carried out on a $81\times81\times21$ k-point grid. It is not possible to compute a strictly static susceptibility. An energy window of 1.0 mRy has been chosen for all calculations. Results obtained using an energy window of 0.1 mRy did not differ significantly. For ground-state calculations in ABINIT, the wave functions were expanded in a plane wave basis with cutoff energy of 40 Hartree. For the trigonal structure, Brillouin zone integration is performed on a 8 $\times8\times4$ Monkhorst-Pack k-point mesh. For the computation of the phonon band structure of the trigonal NbTe$_2$ compound, 35 dynamical matrices have been computed resulting from an unshifted $8\times8\times4$ Monkhorst-Pack Brillouin zone sampling using a cutoff energy of 20 Hartree.

[37] D. Cukjati, A. Prodan, N. Jug, H. van Midden, S. Hla, H. Boehm, F. Boswell, and J. Bennett, Phys. Status Solidi A **193**, 246 (2002).

[38] J. Mesot, M. Randeria, M. R. Norman, A. Kaminski, H. M. Fretwell, J. C. Campuzano, H. Ding, T. Takeuchi, T. Sato, T. Yokoya, T. Takahashi, I. Chong, T. Terashima, M. Takano, T. Mochiku, and K. Kadowaki, Phys. Rev. B **63**, 224516 (2001).

[39] A. Damascelli, Z.-X. Shen, and Z. Hussain, Rev. Mod. Phys. **75**, 473 (2003).

[40] J. Voit, L. Perfetti, F. Zwick, H. Berger, G. Margaritondo, G. Grüner, H. Höchst, and M. Grioni, Science **290**, 501 (2000).

[41] D. Dessau, T. Saitoh, C.-H. Park, Z.-X. Shen, P. Villella, N. Hamada, Y. Moritomo, and Y. Tokura, J. Supercond. **12**, 273 (1999).

[42] L. Perfetti, H. Berger, A. Reginelli, L. Degiorgi, H. Höchst, J. Voit, G. Margaritondo, and M. Grioni, Phys. Rev. Lett. **87**, 216404 (2001).

[43] L. Perfetti, S. Mitrovic, G. Margaritondo, M. Grioni, L. Forró, L. Degiorgi, and H. Höchst, Phys. Rev. B **66**, 075107 (2002).

[44] M. Hohenadler, D. Neuber, W. von der Linden, G. Wellein, J. Loos, and H. Fehske, Phys. Rev. B **71**, 245111 (2005).

[45] S. Sykora, A. Hübsch, K. W. Becker, G. Wellein, and H. Fehske, Phys. Rev. B **71**, 045112 (2005).

[46] P. Kornilovitch, Europhys. Lett. **59**, 735 (2002).

[47] H. H. Weitering, X. Shi, and S. C. Erwin, Phys. Rev. B **54**, 10 585 (1996).

[48] P. Fazekas and E. Tosatti, Philos. Mag. B **39**, 229 (1979).

[49] C. Koitzsch, J. Hayoz, M. Bovet, F. Clerc, L. Despont, C. Ambrosch-Draxl, and P. Aebi, Phys. Rev. B **70**, 165114 (2004).

[50] P. Fazekas and E. Tosatti, Physica B **99**, 183 (1980).

[51] W. McMillan, Phys. Rev. B **14**, 1496 (1976).

[52] G. Ackland, RIKEN Rev. **29**, 34 (2000).

[53] H. Erdogan and R. Kirby, Solid State Commun. **70**, 713 (1989).

[54] M. Mikami, S. Nakamura, M. Itoh, K. Nakajima, and T. Shishido, J. Lumin. **102–103**, 7 (2003).

[55] R. D. King-Smith and D. Vanderbilt, Phys. Rev. B **49**, 5828 (1994).